Fast charging of lithium-ion batteries at all temperatures

Xiao-Guang Yang[a], Guangsheng Zhang[a], Shanhai Ge[a], and Chao-Yang Wang[a,b,c,1]

[a]Electrochemical Engine Center, Department of Mechanical and Nuclear Engineering, The Pennsylvania State University, University Park, PA 16802; [b]National Engineering Laboratory for Electric Vehicles, Beijing Institute of Technology, 100081 Beijing, China; and [c]EC Power, State College, PA 16803

Edited by Alexis T. Bell, University of California, Berkeley, CA, and approved June 1, 2018 (received for review April 24, 2018)

Fast charging is a key enabler of mainstream adoption of electric vehicles (EVs). None of today's EVs can withstand fast charging in cold or even cool temperatures due to the risk of lithium plating. Efforts to enable fast charging are hampered by the trade-off nature of a lithium-ion battery: Improving low-temperature fast charging capability usually comes with sacrificing cell durability. Here, we present a controllable cell structure to break this trade-off and enable lithium plating-free (LPF) fast charging. Further, the LPF cell gives rise to a unified charging practice independent of ambient temperature, offering a platform for the development of battery materials without temperature restrictions. We demonstrate a 9.5 Ah 170 Wh/kg LPF cell that can be charged to 80% state of charge in 15 min even at −50 °C (beyond cell operation limit). Further, the LPF cell sustains 4,500 cycles of 3.5-C charging in 0 °C with <20% capacity loss, which is a 90× boost of life compared with a baseline conventional cell, and equivalent to >12 y and >280,000 miles of EV lifetime under this extreme usage condition, i.e., 3.5-C or 15-min fast charging at freezing temperatures.

lithium-ion battery | fast charging | temperature independent | lithium plating-free | rapid heating

Electric vehicles (EVs) have great promise in addressing climate change and energy security issues (1). Automakers are now lining up to flood the market with a series of new EVs. Despite the rapid drop in cost of lithium-ion batteries (LiBs) by 80% over the last 7 y (2), the EV market still only accounts for ∼1% of annual light-duty vehicle sales. Range anxiety, the fear that an EV may run out of juice on a trip with the driver left stranded, has long been cited as a key reason consumers are reluctant to embrace EVs. This anxiety is compounded by the fact that recharging EVs usually takes much longer than refueling internal combustion engine vehicles (ICEVs). Studies have revealed that annual EV miles traveled increased by >25% in areas where drivers have access to fast charging stations, even in cases where fast charging was used for 1 to 5% of total charging events (3).

An exciting race is going on across the world to boost the number and power of fast charging stations. BMW, Daimler, Ford, and Volkswagen formed a joint venture (4) last year to deploy 400 "ultrafast" charging stations across Europe by 2020, with charging power up to 350 kW, which is able to charge a 200-mile-range EV (e.g., Chevy Bolt with 60-kWh battery) in ∼10 min. Honda has also launched plans to release EVs capable of 15-min fast charging by 2022. Most recently, the US Department of Energy announced funding to support projects for development of extreme fast charging technologies (5), targeting to raise the charging power further to 400 kW.

A critical barrier to fast charging is temperature. To be truly competitive with ICEVs, fast charging of EVs should be region- and weather-independent, the same as refueling a gasoline car. In winter, half of the United States has an average temperature below 0 °C, as shown in Fig. 1*A* (6). None of today's EVs, however, allow fast charging at low temperatures. Nissan Leaf, for instance, can be charged to 80% full in 30 min (∼2-C charge) at room temperature, but would take >90 min (<C/1.5 charge) to charge the same amount of energy at low temperatures, according to their owner's manual (7). This is mainly ascribed to concern about lithium plating. State-of-the-art LiBs typically use graphite as anode material, which has an equilibrium potential within 100 mV vs. Li/Li^+. In harsh conditions, the large anode polarization can push graphite potential below the threshold for lithium plating (8, 9).

A major symptom of lithium plating is a drastic capacity loss, in addition to safety hazards. Indeed, recent data showed that cycle life of LiBs drops considerably with temperature. The commercial 16-Ah graphite/$LiNi_{1/3}Mn_{1/3}Co_{1/3}O_2$ cells in Europe's Mat4Bat project lost 75% capacity in 50 cycles with 1-C charge at 5 °C (10), although the same cells can survive 4,000 cycles at 25 °C. Schimpe et al. (11) cycled identical graphite/$LiFePO_4$ cells at different temperatures. Cells at 25 °C lost 8% capacity in 2,800 equivalent full cycles (EFCs). At the same capacity loss, cell life drops to 1,800 EFCs at 15 °C, 1,400 EFCs at 10 °C, and 350 EFCs at 0 °C. Fig. 1*B* summarizes some recent data (11–15) in the literature on cycle life at different temperatures, normalized by corresponding cycle life at 25 °C. A clear exponential drop of cycle life with temperature can be noted, following the Arrhenius law as proposed by Waldmann et al. (12). Even at a cool temperature of 10 °C, cell life is only about half of that at 25 °C. It is worth noting that 47 out of 50 US states have an average temperature below 10 °C in winter (Fig. 1*A*). Even if averaged annually (*SI Appendix*, Fig. S1), 23 states are below 10 °C. Thus, even when fast charging stations become ubiquitous, consumers are still not able to quickly refuel their EVs for a majority of the year due to the low ambient temperatures.

Fundamentally, lithium plating is affected by the rate of ion conduction and diffusion in the electrolyte, lithium diffusion in graphite particles, and reaction kinetics at graphite surfaces. Key parameters governing these processes all follow the Arrhenius

Significance

Range anxiety is a key reason that consumers are reluctant to embrace electric vehicles (EVs). To be truly competitive with gasoline vehicles, EVs should allow drivers to recharge quickly anywhere in any weather, like refueling gasoline cars. However, none of today's EVs allow fast charging in cold or even cool temperatures due to the risk of lithium plating, the formation of metallic lithium that drastically reduces battery life and even results in safety hazards. Here, we present an approach that enables 15-min fast charging of Li-ion batteries in any temperatures (even at −50 °C) while still preserving remarkable cycle life (4,500 cycles, equivalent to >12 y and >280,000 miles of EV lifetime), thus making EVs truly weather-independent.

Author contributions: X.-G.Y., G.Z., and C.-Y.W. designed research; X.-G.Y., G.Z., and S.G. performed research; X.-G.Y. and C.-Y.W. analyzed data; and X.-G.Y. and C.-Y.W. wrote the paper.

The authors declare no conflict of interest.

This article is a PNAS Direct Submission.

[1]To whom correspondence should be addressed. Email: cxw31@psu.edu.

This article contains supporting information online at www.pnas.org/lookup/suppl/doi:10.1073/pnas.1807115115/-/DCSupplemental.

Published online June 25, 2018.

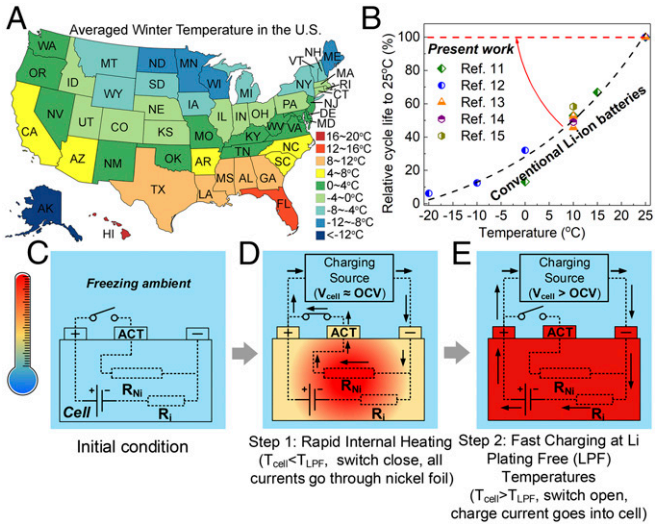

Fig. 1. LPF fast charging independent of ambient temperatures. (*A*) Averaged winter temperature of the United States. Half of them are <0 °C, and 47 states are <10 °C. (*B*) Literature data on cycle life at different temperatures, normalized by cycle life at 25 °C. The LPF cell enables a paradigm shift from the exponential line of conventional Li-ion cells to the top horizontal line. (*C–E*) Schematic illustration of the controllable cell structure for LPF fast charging. The cell, (*C*) initially at a freezing temperature, (*D*) goes through a rapid internal heating step to raise its temperature above a threshold (T_{LPF}) that eliminates lithium plating before (*E*) being charged. Self-heating battery structure is used, which has thin Ni foils inside the cell (refer to *SI Appendix*, Fig. S4 for details). This cell structure enables intelligent control of current partition between Ni foils (heating) and electrode materials (charging) based on cell temperature (T_{cell}). (*D*) If $T_{cell} < T_{LPF}$, switch is closed to direct all current into the Ni foils for rapid heating (~1 °C/s) without going into the anode materials (no plating). (*E*) Once $T_{cell} > T_{LPF}$, switch is opened and all current goes into electrode materials for fast charging without lithium plating.

law and drop substantially with temperature (*SI Appendix*, Fig. S2). As such, a plug-in hybrid EV (PHEV) cell that can withstand a 4-C charge without lithium plating at 25 °C can only allow a 1.5-C charge at 10 °C and C/1.5 at 0 °C to prevent lithium plating (*SI Appendix*, Fig. S3), which explains the long recharge time of today's EVs at low temperatures. To enhance fast charging ability, research in the literature has been focusing on improving anode materials such as coating graphite with an amorphous silicon nanolayer (16, 17) and developing new materials like lithium titanate (18, 19) and graphene balls (20), and on developing new electrolytes (21, 22) and additives (23). LiBs, however, are well known for their trade-off nature among key parameters (24). Improving one property without sacrificing another is always nontrivial. For instance, electrolyte with superior performance at low temperatures is quite often unstable at high temperatures (23, 24). Similarly, decreasing particle size and/or increasing Brunauer–Emmett–Teller (BET) surface area of active materials helps fast charging, but the battery life and safety would suffer. It is extremely difficult, if possible at all, to develop materials with a high rate for charging while preserving durability and safety over a wide range of temperatures.

Here, we make an attempt to free battery science from trade-offs. Specifically, we present a cell structure that can be actively controlled to achieve lithium plating-free (LPF) fast charging in any ambient temperatures, enabling a paradigm shift of the relation between cycle life and temperature (Fig. 1*B*), from the Arrhenius correlation of conventional LiBs to a horizontal line insensitive to temperature. We select 9.5-Ah pouch cells having graphite anode, $LiNi_{0.6}Mn_{0.2}Co_{0.2}O_2$ (NMC622) cathode, and a cell-level energy density of 170 Wh/kg for demonstration. With the LPF cell structure, the cell sustained 4,500 cycles (2,806 EFCs) of 3.5-C charging at 0 °C before reaching 20% capacity loss, which means that, even if an EV is charged once a day in this harsh condition, the LPF cell has a lifetime of 12.5 y and can deliver >280,000 miles of drive range (assuming 1 EFC ≈ 100 miles). That is already beyond the warranty of most ICEVs. For comparison, a conventional LiB cell with identical battery materials at the same testing condition (3.5-C charge at 0 °C) lost 20% capacity in only 50 cycles and 23 EFCs.

Further, this work underscores the concept of unified charging practice independent of ambient temperature. For EVs, battery discharge profiles depend on drivers' behavior, but charging protocols are defined by manufacturers. Today's EVs must reduce charge rate with decreasing temperature due to concern about lithium plating. With the LPF cell, charging from any ambient temperatures is transformed to charging at the optimal temperature in only tens of seconds. As demonstrated here, the LPF cell can be charged to 80% state of charge (SOC) in 15 min even from −50 °C ambient temperature. More profoundly, the charging voltage curve at −50 °C is almost the same as that at 25 °C. This unified charging practice can greatly simply battery management and prolong battery life.

In addition, the LPF cell offers a platform for material scientists. A lingering challenge to battery material research is to find materials that can sustain good performance over a wide range of temperatures. As temperature restrictions are removed with the LPF cells, researchers only need to optimize material performance around a single temperature.

Results and Discussion

Controllable Cell Structure for LPF Fast Charging. The key idea of LPF fast charging is to charge a cell always above a temperature that can prevent lithium plating, hereafter referred to as LPF temperature (T_{LPF}). As illustrated in Fig. 1 *C–E*, a rapid internal heating step (Fig. 1*D*) is added before the charging step (Fig. 1*E*) to make sure that the cell is charged at a temperature above T_{LPF}.

Rapid heating is essential for LPF fast charging, as the overall charge time including heating is limited to 10 min to 15 min. Conventional battery heating methods using external heating devices or thermal management systems are restricted by the intrinsic conflict between heating speed and uniformity (i.e., high heating rate leads to nonuniform temperature and localized overheating near the cell surface), as detailed in ref. 25; thus their heating speed is limited to ~1 °C/min (26), meaning that heating from −20 °C to 20 °C would already take >40 min. Adding the time for charging, it is no longer in the category of fast charging. In this work, we use the self-heating LiB structure (27) which has thin nickel (Ni) foils embedded inside a cell that can create immense and uniform heating, as sketched in *SI Appendix*, Fig. S4. The Ni foil is an inherent component of a single cell along with electrodes and electrolyte. It serves as an internal heating element, as well as an internal temperature sensor as its electrical resistance varies linearly with temperature (*SI Appendix*, Fig. S5). Further, the introduction of Ni foils only adds 0.5% weight and 0.04% cost to a conventional LiB single cell.

A control strategy based on the self-heating battery structure is developed in this work, as illustrated in Fig. 1 *C–E*. The key to this strategy is an intelligent partition of the input current between the Ni foils (heating) and electrode materials (charging) based on cell temperature (T_{cell}). If $T_{cell} < T_{LPF}$ (Fig. 1*D*), a constant voltage close to cell open-circuit voltage (OCV) is applied along with closing the switch between positive and activation terminals. As cell voltage ≈ OCV, all of the current from the charging source is guided to the Ni foils to generate immense internal heat without going into anode materials (no lithium plating). Once $T_{cell} > T_{LPF}$ (Fig. 1*E*), the switch is opened to transit from the heating mode to charging mode, with the current fed to electrode materials without any risk of lithium plating.

We select 9.5-Ah graphite/NMC622 pouch cells for a demonstration of the LPF fast charging. The cells have an areal capacity of 1.85 mAh/cm^2 and a cell-level energy density of 170 Wh/kg. Selection of charge rate and T_{LPF} are based on the simulation results of Li deposition potential (LDP) in *SI*

Appendix, Fig. S3 using a calibrated LiB model. In general, T_{LPF} should be the minimum temperature that can avoid lithium plating at the given charge rate. Although higher temperature is always favorable for eliminating lithium plating, it can also accelerate growth of solid electrolyte interphase (SEI). In this work, a charge rate of 3.5 C and T_{LPF} of ~25 °C are selected based on *SI Appendix*, Fig. S3*C*.

Fig. 2 shows the overall LPF fast charging process of the 9.5-Ah cell from an extreme temperature of −40 °C. Before the test, the fully discharged cell was soaked in an environmental chamber at −40 °C for >12 h. To ensure that the cell was not charged (no lithium plating) in the heating step, a voltage of 3.15 V, slightly lower than OCV (~3.2 V), was applied along with closing the switch (referring to Fig. 1*D*). As such, all of the input current went through the Ni foils (Fig. 2*E*) automatically, without going into battery materials. As the cell voltage was set to be 50 mV lower than OCV, the cell was slightly discharging in the heating step, which gradually increased to ~0.2 C toward the end when the cell became warmed up (Fig. 2*F*). Nonetheless, the total discharge capacity during the heating step only amounts to 6.85×10^{-3} Ah or 0.072% of cell capacity and hence is negligibly inconsequential. With the huge current flowing into the Ni foils, the cell was heated up rapidly (Fig. 2*C*). Once surface temperature reached 20 °C, the switch was opened to complete the heating step, and the cell then rested 10 s for relaxation of the internal temperature gradient. As shown in Fig. 2*G*, the Ni foil temperature, the highest temperature inside the cell, was <45 °C during heating and quickly dropped and met with surface temperature at ~27 °C after the 10-s rest period, indicating that there is no safety concern regarding the rapid heating. Thereafter, the cell switched to charge mode using constant current constant voltage (CCCV) protocol at a current of 3.5 C limited by a cutoff voltage of 4.2 V until reaching 80% SOC. The whole process took 894.8 s (14.9 min), including 61.6 s of heating and 10 s of thermal relaxation.

For comparison, an identical baseline cell was charged without the rapid heating step using the same CCCV protocol at −40 °C (*SI Appendix*, Fig. S6). Due to the extremely sluggish electrochemical kinetics and electrolyte transport and hence high internal resistance, cell voltage touched the 4.2-V limit immediately upon charging (*SI Appendix*, Fig. S6*A*), and the starting current was only ~0.2 C (*SI Appendix*, Fig. S6*B*). The charging current recovered slowly with the sluggish rise of temperature (*SI Appendix*, Fig. S6*C*) due to the limited heat generation rate. The maximum charging current was only 0.85 C, and it took 115 min to reach 80% SOC, which is 7.7× of the LPF cell.

In general, at very low temperatures, it may be possible to develop a battery to discharge a reasonable percent of capacity; however, it is virtually impossible to charge the battery at a reasonable rate. This stems from the asymmetric electrochemical kinetics of charging versus discharging prevalent in electrochemistry. On the other hand, applications usually demand a higher rate of charging for time saving. The method of heating–charging via the self-heating battery structure presented herein is able to decouple the charge and discharge processes by rapid modulation of internal temperature; thus it is able to overcome poorer electrochemical kinetics of charging than discharging for a wide array of electrochemical energy storage cells.

Unified Charging Curve Independent of Ambient Temperature. Fig. 3 compares charging of the 9.5-Ah LPF cell at different ambient temperatures (−50 °C, −40 °C, −20 °C, and 0 °C). The testing

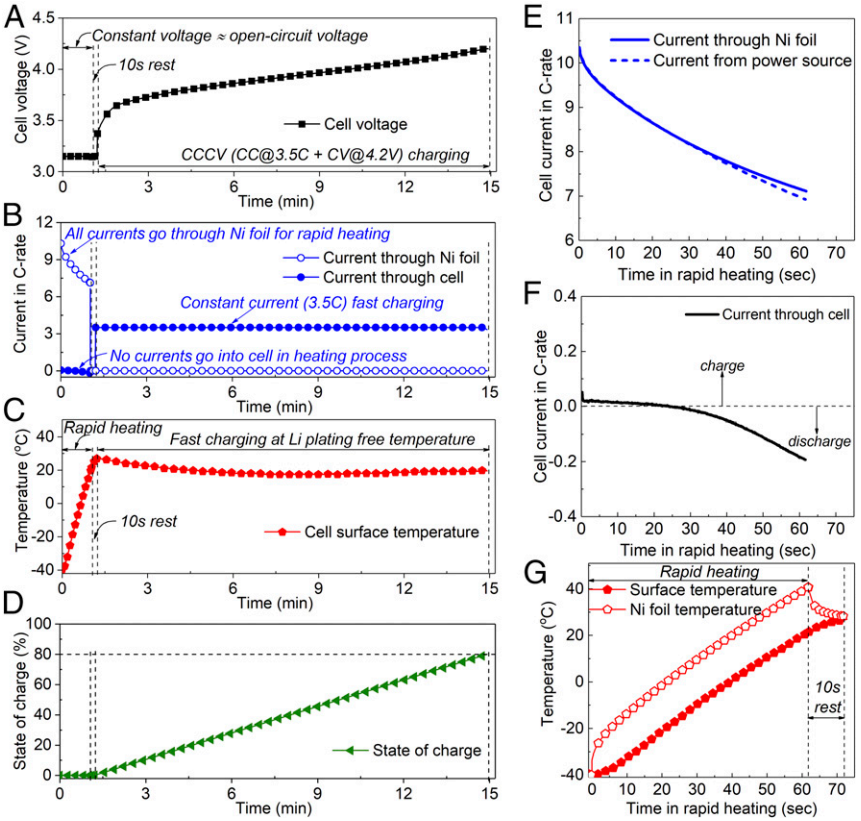

Fig. 2. The 15-min fast charging at −40 °C. (*A*–*D*) Evolutions of (*A*) cell voltage, (*B*) current partition between nickel (Ni) foils and cell, (*C*) surface temperature, and (*D*) SOC. The cell was initially at 0% SOC and −40 °C, with an OCV of ~3.2 V. The whole charging process was divided into a rapid internal heating step, followed by a 10-s rest and then CCCV charging (3.5 C, 4.2 V) until reaching 80% SOC. (*E* and *F*) Intelligent control of current partition between Ni foils and electrode materials in the heating process. (*E*) All input current goes into the Ni foils and (*F*) negligible current goes into the anode materials (no plating) in the heating step. (*G*) Evolutions of surface and Ni foil temperatures during the heating and relaxation steps.

protocol was the same in all cases: (*i*) fully discharging at 25 °C and then cooling down to the testing temperature; (*ii*) rapidly heating by applying a constant voltage of 3.15 V until surface temperature is >20 °C; (*iii*) 10-s relaxation; and (*iv*) CCCV charging (3.5 C, 4.2 V) to 80% SOC. It can be seen that the voltage curves are almost the same in all cases despite the huge difference in ambient temperature (Fig. 3*A*). It took 69 s to heat the cell from −50 °C to 20 °C (~1 °C/s) and 30.2 s from 0 °C to 20 °C (0.66 °C/s). The faster heating at lower ambient temperature benefited from the reduction of Ni foil resistance with temperature (*SI Appendix*, Fig. S5), leading to higher heating current at lower temperature (Fig. 3*C*). Even in the case of −50 °C, the heating step only accounted for 7.6% of the time of the entire process. The total time to charge the cell to 80% SOC was similar in all four cases (Fig. 3*B*, 905.7 s at −50 °C and 863.2 s at 0 °C, ~5% difference). Thereby, the strong restrictions of ambient temperature on charging time, as in all of today's EVs, is totally removed with the LPF cell.

Both surface and Ni foil temperatures reached ~27 °C after the 10-s thermal relaxation (*SI Appendix*, Fig. S7) in all four cases, indicating that the starting point of charging is similar. Thus, the voltage curves in the subsequent CCCV charging were quite similar (*SI Appendix*, Fig. S8*A*). The slightly higher voltage at lower ambient temperature was ascribed to the larger temperature drop during charging (*SI Appendix*, Fig. S8*B*), due to the strong cooling in the environmental chamber. With better thermal insulation and management, it is reasonable to expect that the charging curve can become unified and independent of ambient temperature. A unified charge curve could greatly simplify the battery management system and enhance the accuracy of battery state estimation (SOC, state of health, etc.) and hence is extremely useful for EVs.

It should be noted that today's EVs, in principle, can also be heated to $>T_{LPF}$ before charging, using thermal management systems outside single cells; however, the intrinsically low speed of external heating (<1 °C/min) makes it impossible to tackle the problem of fast charging. Further, as automotive cells are becoming bigger and thicker to reduce the manufacturing cost, the speed of external heating should be further reduced to avoid localized overheating on the cell surface (25). Our method of inserting Ni foils enables rapid and uniform internal heating no matter how large the cell is (heating uniformity can be guaranteed by adding multiple Ni foils). The method can also be applied to other cell geometries. For instance, Ni foil can form a sleeve wrapped around the first half of a cylindrical jelly roll before the second half is wound, thus placing it right in the middle of a jelly roll for a cylindrical cell. Several examples of Ni foil designs for various types and form factors of cells can be found in ref. 28. Furthermore, the flow of current inside the cell, between the heating element and battery materials, is actively controllable, enabling seamless switching between the rapid heating mode and charging mode based on cell temperature. Even in the extreme case of −50 °C where the electrolyte already ceases to work, the LPF cell is still charged to 80% SOC in 15 min, just as at room temperature, further demonstrating its potential to make EVs truly region- and weather-independent.

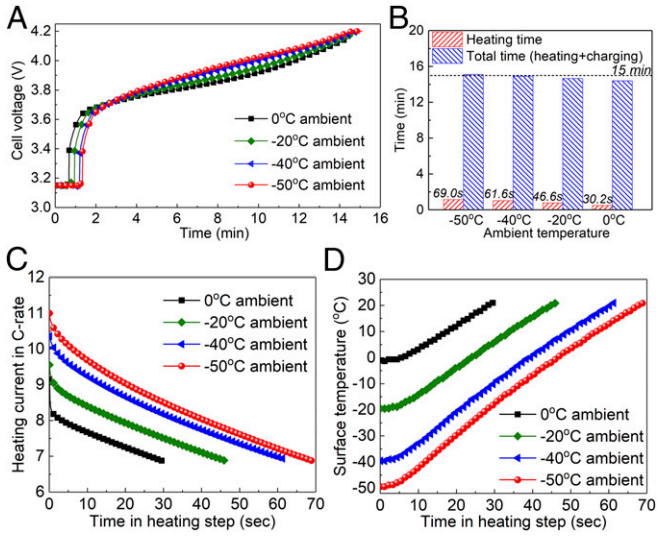

Fig. 3. Unified charging practice independent of ambient temperature. (*A*) Voltage curves of the LPF cell at different ambient temperatures. In all of the tests, the cell went through a rapid heating step at 3.15 V until reaching surface temperature of >20 °C, rested for 10 s, and then was charged at a constant current of 3.5 C followed by constant voltage of 4.2 V until reaching 80% SOC. (*B*) Summary of heating time and total time, demonstrating that restrictions of ambient temperature on charge time are eliminated. (*C* and *D*) Evolutions of (*C*) current through nickel foils and (*D*) cell surface temperature in the rapid heating step.

Remarkable Cycle Life by Elimination of Lithium Plating. We further demonstrate the elimination of lithium plating in the LPF cell. Charging of the LPF cell at 0 °C is compared with two baseline conventional cells with identical materials and electrodes, which were charged with the same CCCV (3.5 C, 4.2 V) protocol to 80% SOC without the heating step. One baseline cell was tested at 0 °C, and the other was tested at 25 °C. As shown in Fig. 4*A*, the voltage curve of the LPF cell at 0 °C after the rapid heating step almost overlapped with that of the baseline cell at 25 °C, with a very slight difference due to the difference in temperature (Fig. 4*B*). The baseline cell at 0 °C, however, has much higher voltage than the other two cells due to its high internal resistance. All three cells were left at open circuit after charging to 80% SOC, and the voltage curves during relaxation are compared in Fig. 4*C*. A clear voltage plateau is observed in the relaxation curve of the baseline cell at 0 °C, leading to a local peak in the differential voltage curve (Fig. 4*D*). The voltage plateau and peak of differential voltage indicate the occurrence of Li metal stripping, and thus are clear evidence that lithium plating occurred in the 3.5-C charging of the baseline cell at 0 °C. In the other two cases, cell voltage drops rapidly to a relatively stable value, indicating that no lithium plating occurred during charging.

Eliminating lithium plating significantly boosted cycle life at low temperatures. Cycling tests were performed with 3.5-C charging to 4.2 V followed by a 2-min rest and then 1-C discharge to 2.7 V. For the LPF cell, a rapid heating step at a constant voltage of 3.4 V was performed in the beginning of each cycle and completed at $T_{cell} > 20$ °C, followed by 10-s relaxation. Cells were cooled down fully to 0 °C after the discharge step before starting the next cycle. Evolutions of voltage and temperature during cycling are given in *SI Appendix*, Fig. S9 (one cycle) and *SI Appendix*, Fig. S10 (10 cycles). Discharge capacity of each cycle is given in *SI Appendix*, Fig. S11. Cycling tests were paused periodically for calibration of cell capacity with reference performance test (RPT) at 25 °C (*SI Appendix*, Fig. S12). The measured C/3 discharge capacity in RPT was plotted against cycle number in Fig. 4*E* for both the baseline and LPF cells. The baseline cell lost 20% capacity in only 50 cycles, whereas the LPF cell sustained 4,500 cycles at the same capacity retention, which is a 90× boost in cycle life. Even if EV drivers perform fast charging once a day, 4,500 cycles mean 12.5 y of operation. Converting to EFCs (i.e., total capacity discharged during cycling divided by nominal capacity 9.5 Ah), 2,806 EFCs were achieved at 80% capacity retention, which is a 122× boost compared with the baseline cell (23 EFCs). Assuming 100-mile driving range per EFC (e.g., BMW i3), 2,806 EFCs indicate >280,000 miles of lifetime, far beyond the warranty of today's ICEVs.

The above two cells in Fig. 4*E* are further compared with additional baseline cells, one cycled at 10 °C and one cycled at 22 °C. These two baseline cells were initially at 20% SOC and charged and discharged by a fixed amount of capacity that equals 60% SOC of fresh cell in each cycle, with CCCV (3 C, 4.2 V)

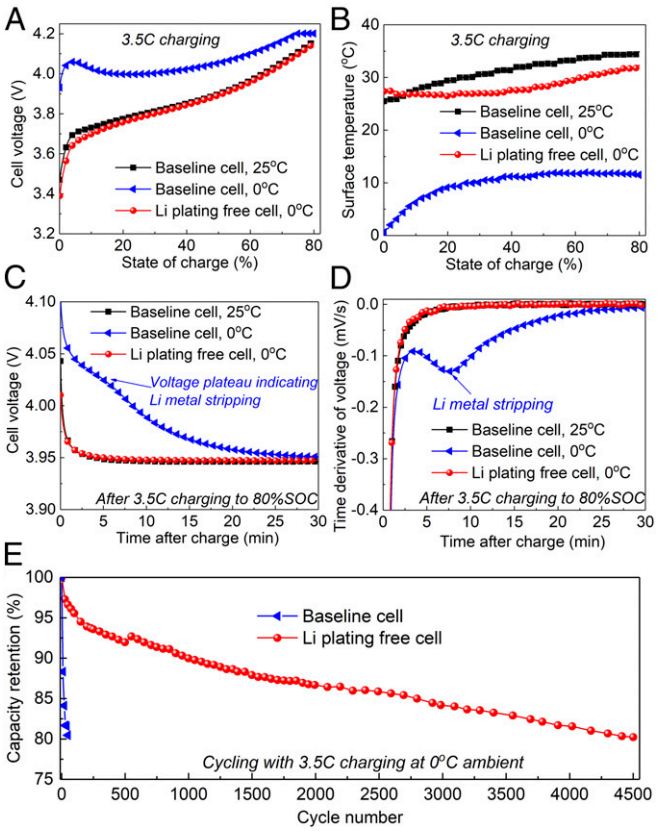

Fig. 4. Remarkable cycle life of the LPF cell. Comparison of baseline cells at 0 °C and 25 °C with the LPF cell at 0 °C in terms of (*A*) voltage and (*B*) surface temperature during charging and (*C*) voltage and (*D*) time derivative of voltage during cell relaxation after charging. All cells were charged with 3.5-C current limited by 4.2 V until they reached 80% SOC. The voltage plateau in *C* and the local peak of differential voltage in *D* of the baseline cell at 0 °C indicate lithium metal stripping. (*E*) Capacity retention vs. cycle number for an LPF cell and a baseline cell cycling with 3.5-C charging at 0 °C ambient temperature.

charge and 1-C discharge. As cycling protocols are somewhat different, capacity retentions of these cells are plotted against EFC in Fig. 5*A*. We note that the cell with 3-C charging at 10 °C only lasted 317 EFCs at 80% capacity retention. Moreover, the LPF cell at 0 °C has an even longer cycle life than the baseline cell at 22 °C. The reason is twofold. First, as lithium plating is eliminated, the dominant aging mechanism is SEI growth, which depends primarily on temperature. As shown in *SI Appendix*, Fig. S10*B*, the discharge and cooling portions of the LPF cell were below 22 °C. The average temperature of the LPF cell in the 10 cycles shown in *SI Appendix*, Fig. S10*B* is 11.6 °C, far lower than the average temperature of the baseline cell (~28 °C). As such, the SEI growth in the LPF cell was, overall, slower than that in the baseline cell. Second, the baseline cell was charged by a fixed amount of capacity in each cycle, which equaled 60% SOC of the fresh cell but became larger than 60% SOC as the cell degraded. Thus, the baseline cell was charged to higher SOC than the LPF cell (charged to 4.2 V, no constant voltage step) in the late stage of cycling. The higher SOC would also lead to faster SEI growth.

Fig. 5*B* further compares the aging rate of the above four cases, which is defined as the ratio of capacity loss (in percent) to EFC at the end of life, and plotted in log scale against reciprocal temperature. For baseline cells, the logarithm of aging rate vs. 1/T can be fitted with a linear line, confirming that the aging rate of conventional LiBs follows Arrhenius law (12). The activation energy is estimated to be −1.37 eV, which is within the range reported in the literature (29). We note that the aging rate of the LPF cell at 0 °C was brought down by two orders of magnitude compared with the baseline conventional cell, and became close to that of the baseline cell at room temperature, indicating a paradigm shift of the relationship between aging rate and ambient temperature.

LPF Fast Charging of High-Energy Cells by Elevated Temperature. For future long-range EVs, a system-level energy density of at least 225 Wh/kg is demanded, which requires cell-level energy density to be >300 Wh/kg (30). A typical approach to raise cell-level energy density is to increase the areal capacity (and thickness) of electrodes. Cells with thicker anodes, however, are more prone to lithium plating due to larger electrolyte transport resistance. Recent work (30) showed that a graphite/NMC622 pouch cell with an areal loading of 3.3 mAh/cm^2, ~1.8× of the PHEV cell in this work, lost 22.5% capacity in 52 cycles of 1.5-C charge at 30 °C. A large amount of lithium metal was observed after dismantling the aged cell, indicating that lithium plating can be a serious issue in the high-energy (HE) cells even around room temperature.

A feasible approach to eliminate lithium plating in the HE cells is to further increase charging temperature. As shown in *SI Appendix*, Fig. S2, increasing from 25 °C to 45 °C boosts lithium intercalation kinetics by 5.6×, lithium diffusivity in graphite by 2.4×, and electrolyte conductivity by 1.4×, and hence can help alleviate lithium plating. *SI Appendix*, Fig. S13 shows the model-predicted LDP of an HE cell having 1.65× areal capacity and thickness of the PHEV cell in this work. We note that the maximum charge current at 25 °C without lithium plating drops from 4 C for the PHEV cell (*SI Appendix*, Fig. S3*C*) to ~1.5 C for the HE cell (*SI Appendix*, Fig. S13*A*) due to the increased electrode thickness. If charging the cell at 45 °C, the maximum charge rate of the HE cell can be raised to 3 C. Indeed, recent studies have shown that cells with thick electrodes have a longer cycle life at 40 °C to 45 °C than at room temperature. Jossen's group (31) reported that a graphite/$LiCoO_2$ cell with a 77-μm-thick anode (1.6× of present work) lost 30% capacity in 250

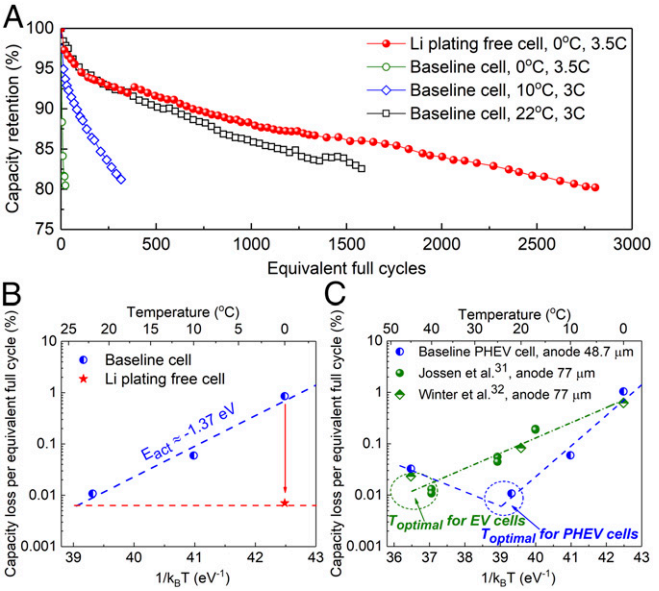

Fig. 5. Paradigm shift of ambient temperature effects on cell aging. (*A*) Cycle life comparison of the LPF cell with 3.5-C charging at 0 °C with same baseline cells at different temperatures. (*B*) Aging rate vs. reciprocal temperature of the four cells in *A*. Aging rate is defined as the ratio of capacity loss (in percent) to EFC at the end of life, and is plotted in log scale. (*C*) Aging rate of next-generation HE cells (with thick electrode) in the literature. The optimal charging temperature of HE EV cells shifts from ~25 °C for current PHEV cells to ~40 °C to 50 °C.

cycles with 1-C charge at 25 °C, but only lost 5% capacity after 400 cycles at 40 °C. Similarly, Winter's group (32) found that the cycle life of a graphite/NMC532 cell with a 77-μm-thick anode increased from 400 cycles at 20 °C to 1,100 cycles in 45 °C at 70% capacity retention. Most recently, researchers from Samsung (20) developed an HE cell with 5-C charging capability at 60 °C.

Fig. 5*C* compares the aging rate of the above HE cells with the PHEV cells in this work. The aging rate of the PHEV cell at 45 °C is also added. As reported in the literature (33), cell aging is a combined effect of SEI growth and lithium plating. For the PHEV cell, 25 °C is high enough to prevent lithium plating at the charge rate of 3.5 C (*SI Appendix*, Fig. S3). Further increasing to 45 °C reduced the cycle life to ∼613 EFCs at 80% capacity retention due to faster SEI growth. For the HE cells, however, it is beneficial to operate at ∼40 °C to 45 °C due to the alleviation of lithium plating, which outpaces the negative impacts of faster SEI growth. Hence, operating at higher temperatures can be a promising approach to enhance the life of HE cells. In this regard, heating would be an essential step for the charging of HE cells. Given the inherently low speed of external heating, the present LPF cell holds great promise for next-generation EVs, as it can modulate cell internal temperature almost instantaneously on demand.

In broad perspectives, the scientific merit of the LPF cell described herein is that it offers a general solution to decouple charge kinetics from discharge in battery science, and to accelerate battery charging without demanding new material or chemistry. It also offers a platform for material scientists to develop more advanced battery materials without temperature concern. On the application side, the present work permanently removes the longstanding restrictions of ambient temperature on battery charging, enabling a vast array of new electronics and devices such as all-weather smartphones, outdoor robots, drones and microsatellites working at high altitudes, as well as new applications such as rescuing vehicles stranded in snow, and explorations in the space and Arctic.

Methods and Materials

The 9.5-Ah LPF pouch cells were fabricated with NMC622 as cathode, graphite as anode, and 1 M $LiPF_6$ dissolved in ethylene carbonate (EC)/ethyl methyl carbonate (EMC) (3:7 by wt.) + 2 wt% vinylene carbonate (VC) as electrolyte. The cells have an areal capacity of 1.85 mAh/cm^2 and a cell-level energy density of 170 Wh/kg. Each LPF cell has two pieces of Ni foil embedded inside, as sketched in *SI Appendix*, Fig. S4. Each Ni foil, having a thickness of 30 μm and a resistance of 80.2 mΩ at 25 °C, is coated with thin (28 μm) polyethylene terephthalate for electrical insulation and sandwiched between two single-sided anode layers. The two three-layer assemblies are stacked inside the cell and connected in parallel, with one assembly located at 1/4 cell thickness and the other at 3/4 cell thickness from the top cell surface. More details about cell materials, fabrication, structure, and testing can be found in *SI Appendix, Methods and Materials*.

ACKNOWLEDGMENTS. Financial support by Pennsylvania Department of Environmental Protection; EC Power, LLC; and US Department of Energy under Award DE-EE0006425 is gratefully acknowledged. We are also grateful to EC Power for offering AutoLion software, which has been acquired by Gamma Technologies.

1. Needell ZA, McNerney J, Chang MT, Trancik JE (2016) Potential for widespread electrification of personal vehicle travel in the United States. *Nat Energy* 1:16112.
2. Bloomberg New Energy Finance (2018) Electric vehicle outlook 2018, Available at https://about.bnef.com/electric-vehicle-outlook/#toc-download. Accessed May 25, 2018.
3. Lutsey N, Searle S, Chambliss S, Bandivadekar A (2015) *Assessment of Leading Electric Vehicle Promotion Activities in United States Cities* (Int Counc Clean Transp, Washington, DC).
4. Ionity (2017) Joint venture of BMW, Daimler, Ford and Volkswagen for deploying fast charging stations. Available at www.ionity.eu/ionity-en.html. Accessed May 25, 2018.
5. Energy.gov (2018) Department of Energy announces $19 million funding for development of extreme fast charging technologies. Available at https://www.energy.gov/articles/department-energy-announces-19-million-advanced-battery-and-electrification-research-enable. Accessed May 25, 2018.
6. Current Results (2018) Winter temperature averages for every state. Available at https://www.currentresults.com/Weather/US/average-state-temperatures-in-winter.php. Accessed May 25, 2018.
7. Nissan (2017) Nissan Leaf owner's manual. Available at https://cdn.dealereprocess.net/cdn/servicemanuals/nissan/2017-leaf.pdf. Accessed May 25, 2018.
8. Wandt J, Jakes P, Granwehr J, Eichel R-A, Gasteiger HA (2018) Quantitative and time-resolved detection of lithium plating on graphite anodes in lithium ion batteries. *Mater Today* 21:231–240.
9. Li Z, Huang J, Yann Liaw B, Metzler V, Zhang J (2014) A review of lithium deposition in lithium-ion and lithium metal secondary batteries. *J Power Sources* 254:168–182.
10. Matadi BP, et al. (2017) Irreversible capacity loss of Li-ion batteries cycled at low temperature due to an untypical layer hindering Li diffusion into graphite electrode. *J Electrochem Soc* 164:A2374–A2389.
11. Schimpe M, et al. (2018) Comprehensive modeling of temperature-dependent degradation mechanisms in lithium iron phosphate batteries. *J Electrochem Soc* 165:A181–A193.
12. Waldmann T, Wilka M, Kasper M, Fleischhammer M, Wohlfahrt-Mehrens M (2014) Temperature dependent ageing mechanisms in lithium-ion batteries–A post-mortem study. *J Power Sources* 262:129–135.
13. Wang J, et al. (2014) Degradation of lithium ion batteries employing graphite negatives and nickel–cobalt–manganese oxide + spinel manganese oxide positives: Part 1, aging mechanisms and life estimation. *J Power Sources* 269:937–948.
14. Reichert M, et al. (2013) Influence of relaxation time on the lifetime of commercial lithium-ion cells. *J Power Sources* 239:45–53.
15. Ecker M, Shafiei Sabet P, Sauer DU (2017) Influence of operational condition on lithium plating for commercial lithium-ion batteries—Electrochemical experiments and post-mortem-analysis. *Appl Energy* 206:934–946.
16. Kim N, Chae S, Ma J, Ko M, Cho J (2017) Fast-charging high-energy lithium-ion batteries via implantation of amorphous silicon nanolayer in edge-plane activated graphite anodes. *Nat Commun* 8:812.
17. Park M-H, et al. (2014) Flexible high-energy Li-ion batteries with fast-charging capability. *Nano Lett* 14:4083–4089.
18. Odziomek M, et al. (2017) Hierarchically structured lithium titanate for ultrafast charging in long-life high capacity batteries. *Nat Commun* 8:15636.
19. Wang S, et al. (2017) Lithium titanate hydrates with superfast and stable cycling in lithium ion batteries. *Nat Commun* 8:627.
20. Son IH, et al. (2017) Graphene balls for lithium rechargeable batteries with fast charging and high volumetric energy densities. *Nat Commun* 8:1561.
21. Yamada Y, Yaegashi M, Abe T, Yamada A (2013) A superconcentrated ether electrolyte for fast-charging Li-ion batteries. *Chem Commun (Camb)* 49:11194–11196.
22. Yamada Y, et al. (2014) Unusual stability of acetonitrile-based superconcentrated electrolytes for fast-charging lithium-ion batteries. *J Am Chem Soc* 136:5039–5046.
23. Smart MC, Ratnakumar BV (2011) Effects of electrolyte composition on lithium plating in lithium-ion cells. *J Electrochem Soc* 158:A379–A389.
24. Rodrigues M-TF, et al. (2017) A materials perspective on Li-ion batteries at extreme temperatures. *Nat Energy* 2:17108.
25. Yang XG, Liu T, Wang CY (2017) Innovative heating of large-size automotive Li-ion cells. *J Power Sources* 342:598–604.
26. Ji Y, Wang CY (2013) Heating strategies for Li-ion batteries operated from subzero temperatures. *Electrochim Acta* 107:664–674.
27. Wang CY, et al. (2016) Lithium-ion battery structure that self-heats at low temperatures. *Nature* 529:515–518.
28. Wang CY, Ge S (2018) US Patent 9,882,197.
29. Arai J, Nakahigashi R (2017) Study of Li metal deposition in lithium ion battery during low-temperature cycle using in situ solid-state 7Li nuclear magnetic resonance. *J Electrochem Soc* 164:A3403–A3409.
30. Gallagher KG, et al. (2016) Optimizing areal capacities through understanding the limitations of lithium-ion electrodes. *J Electrochem Soc* 163:A138–A149.
31. Rieger B, et al. (2016) Multi-directional laser scanning as innovative method to detect local cell damage during fast charging of lithium-ion cells. *J Energy Storage* 8:1–5.
32. Friesen A, et al. (2016) Impact of cycling at low temperatures on the safety behavior of 18650-type lithium ion cells: Combined study of mechanical and thermal abuse testing accompanied by post-mortem analysis. *J Power Sources* 334:1–11.
33. Yang XG, Leng Y, Zhang G, Ge S, Wang CY (2017) Modeling of lithium plating induced aging of lithium-ion batteries: Transition from linear to nonlinear aging. *J Power Sources* 360:28–40.

Supplementary Information Appendix for

Fast Charging of Lithium-ion Batteries at All Temperatures

Xiao-Guang Yang[a], Guangsheng Zhang[a], Shanhai Ge[a] and Chao-Yang Wang[a,b,c,1]

[a] Department of Mechanical and Nuclear Engineering and Electrochemical Engine Center (ECEC), The Pennsylvania State University, University Park, Pennsylvania 16802, USA.

[b] National Engineering Laboratory for Electric Vehicles, Beijing Institute of Technology, Beijing 100081, China

[c] EC Power, 341 Science Park Road, State College, Pennsylvania 16803, USA.

[1]Corresponding author, email: cxw31@psu.edu

This PDF file includes:

www.pnas.org/cgi/doi/10.1073/pnas.1807115115

Methods and Materials

Cell materials and fabrication

9.5Ah pouch cells are fabricated with $LiNi_{0.6}Mn_{0.2}Co_{0.2}O_2$ (NMC622) as cathode, graphite as anode, 1M of $LiPF_6$ dissolved in EC/EMC (3:7 by wt.)+2wt% VC as electrolyte, and Celgard-2325 microporous tri-layer membrane as separator. The cathodes are prepared by coating NMP based slurry onto 15 μm thick Al foil, whose dry material consists of NMC622 (91.5 wt%), Super-C65 (Timcal) (4.4 wt%) and PVdF (Hitachi) (4.1 wt%) as a binder. The anodes are prepared by coating deionized (DI) water-based slurry onto 10 μm thick Cu foil, whose dry material consists of graphite (95.4 wt%), Super-C65 (1.0 wt%), SBR (JSR) (2.2 wt%) and CMC (Nippon Paper) (1.4 wt%). The mass loading of NMC622 cathode and graphite anode are 10.574 mg/cm^2 and 6.678 mg/cm^2, corresponding to 1.85 mAh/cm^2 and 2.23 mAh/cm^2, respectively. After calendaring, the cathode and anode thickness (single-side) are 40.75 μm and 48.7 μm. Each pouch cell consists of 34 anode and 33 cathode layers, with 152×75 mm footprint area, 9.5Ah nominal capacity (relative to which all C-rates are defined), and cell-level specific energy of 170 Wh/kg and 334 Wh/L.

Each lithium plating free (LPF) cell has two pieces of Ni foils embedded inside, as sketched in *SI Appendix*, Fig. S4. Each Ni foil has a thickness of 30 μm and a resistance of 80.2 mΩ at 25^{o}C, and is coated with thin (28 μm) polyethylene terephthalate for electrical insulation, and sandwiched between 2 single-sided anode layers. The two 3-layer assemblies are then stacked inside the cell, with one assembly located at ¼ cell thickness and the other at ¾ cell thickness from the top cell surface. One ends of the two Ni foils are welded with tabs of anode layers and connected to the negative terminal; the other ends of the two Ni foils are welded and extend outside to form a third terminal. The Ni foil resistance (*SI Appendix*, Fig. S5) in this work refers to the total resistance of the two Ni sheets connected in parallel.

Cell tests

Prior to each fast charging test (Figs. 2-3), the cell was discharged at 25^{o}C with C/3 rate to 2.7V, and then put in a thermal insulation box and soaked in an environmental chamber at testing temperature for >12 hours to reach thermal equilibrium. All tests were performed with Arbin BT-2000. For tests of the LPF cell, current through Ni foils (Fig. 2E) was measured with a 0.75 mΩ shunt resistor connected in between positive and ACT terminals, and cell current (Fig. 2F) was calculated as Ni foil current minus current from Arbin. Ni foil resistance is calculated by the voltage difference between ACT and negative terminals divided the Ni foil current.

Electrochemical-Thermal Coupled Simulation

Electrochemical-thermal coupled modeling is performed with a commercial simulation package-AutoLion^{TM} 1D. Material properties of graphite anode, NMC622 cathode and electrolyte are taken from the built-in database of AutoLion. The model is first calibrated with experimental data of the 9.5Ah cell in terms of charge and discharge curves at different C-rates and temperatures, and then used to predict the lithium deposition potential (LDP) in the charging process at different C-rates and temperatures (*SI Appendix*, Fig. S3). The LDP is defined as φ_s-φ_e-I*R_{SEI} at the anode/separator interface, with φ_s being electronic potential, φ_e the electrolyte potential, I the local current density and R_{SEI} the resistance of SEI layer. Lithium plating is expected to occur at LDP<0V. The model is extended to predict the LDP of a HE cell in *SI Appendix*, Fig. S13, which has the same footprint as the PHEV cell, with 1.65x areal loading and thickness in both the anode and cathode, and a total of 21 anode layers and 20 cathode layers. The nominal capacity of the HE cell is also 9.5Ah. All other parameters are kept the same as the PHEV case.

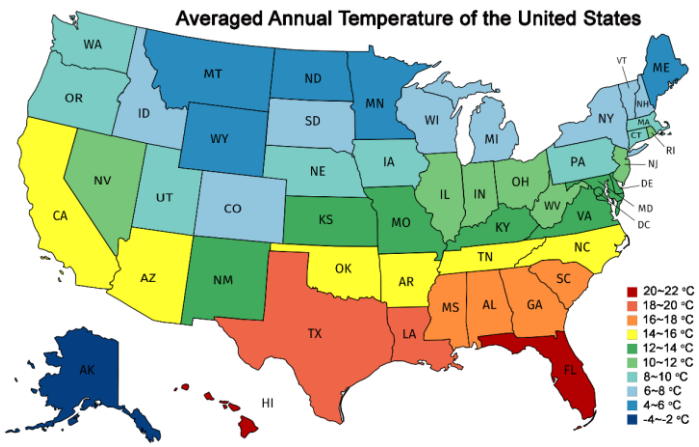

Figure S1. Averaged annual temperature of the United States.

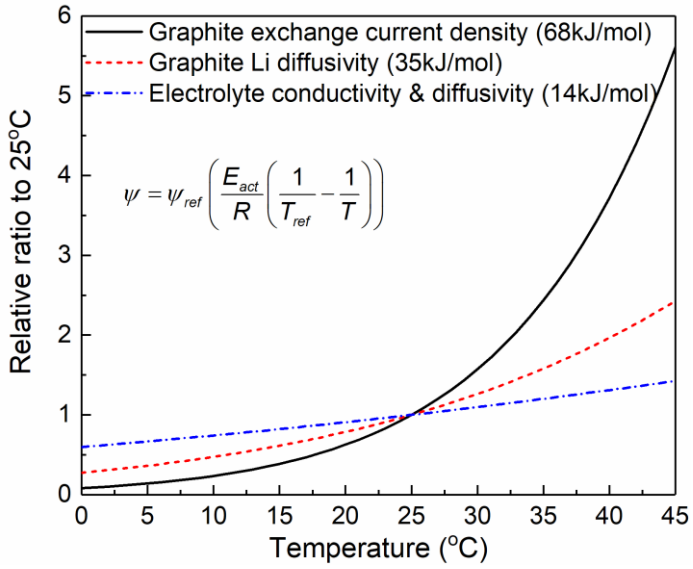

Figure S2. Arrhenius-type temperature dependence of key parameters affecting fast charging capability, including the anode exchange current density, solid-state diffusivity in graphite particles, electrolyte conductivity and diffusivity.

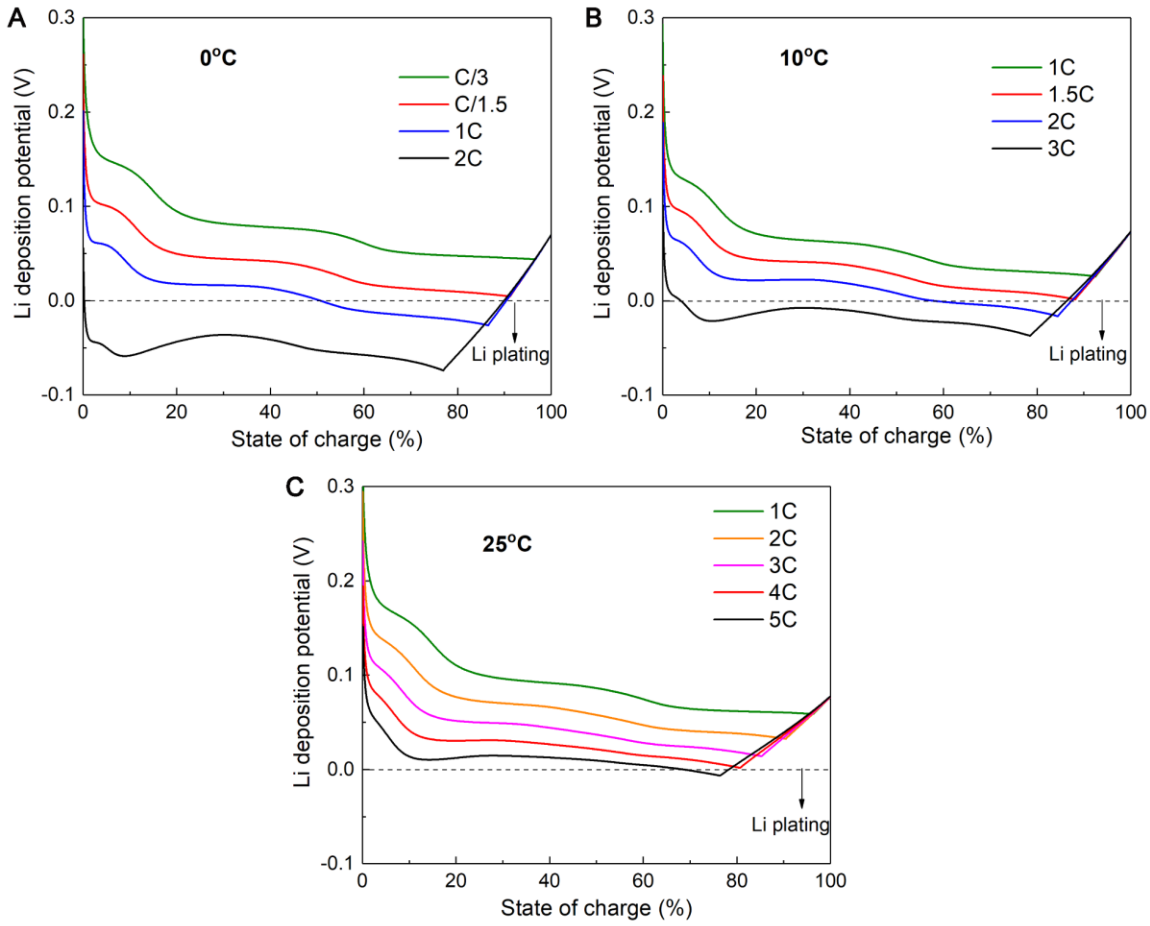

Figure S3. Maximum charge rate at different temperatures for a plug-in hybrid electric vehicle (PHEV) cell. Simulation results of the lithium deposition potential (LDP) during charging of a 9.5Ah PHEV cell with different C-rates at different temperatures **(A)** 0°C, **(B)** 10°C and **(C)** 25°C. Lithium plating is expected to occur when LDP<0V. The maximum charge rate without lithium plating drops from 4C at 25°C to 1.5C at 10°C and C/1.5 at 0°C.

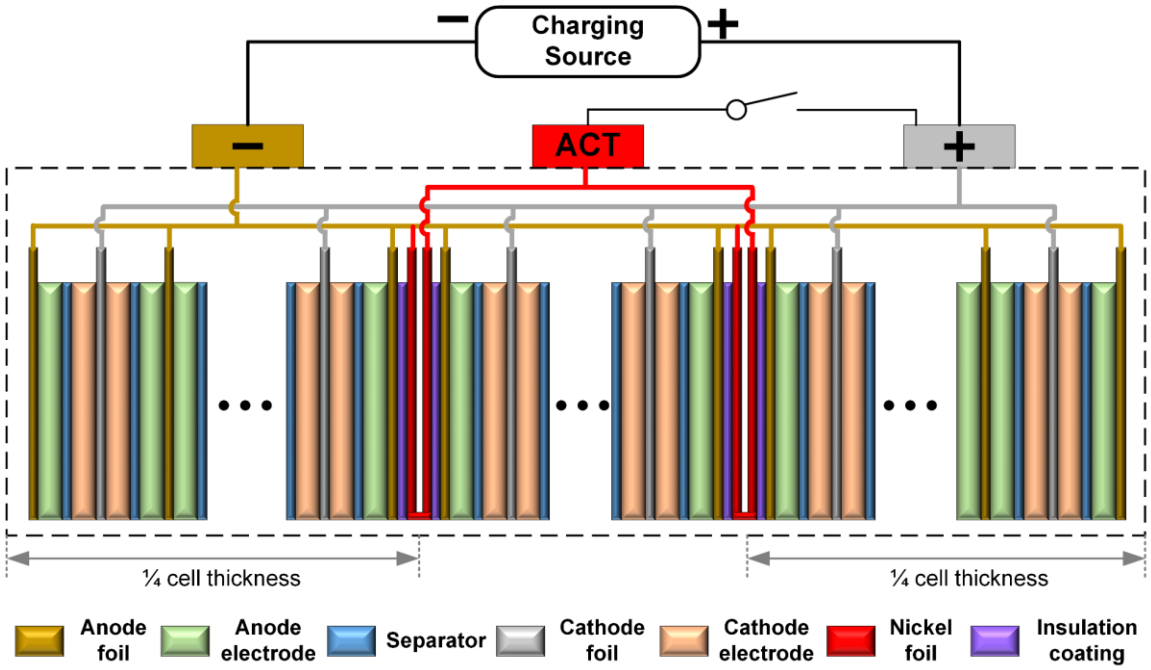

Figure S4. Schematic of the self-heating lithium-ion battery structure. Two pieces of thin nickel (Ni) foils are inserted into the cell, each located at ¼ cell thickness from cell surfaces. Each Ni foil is coated with thin polyethylene terephthalate for electrical insulation, and sandwiched between 2 single-sided anode layers. One ends of the two Ni foils are welded with tabs of anode layers and connected to the negative terminal; the other ends of the two Ni foils are welded and extend outside to form a third terminal, named activation (ACT) terminal. A switch is added between positive and ACT terminals.

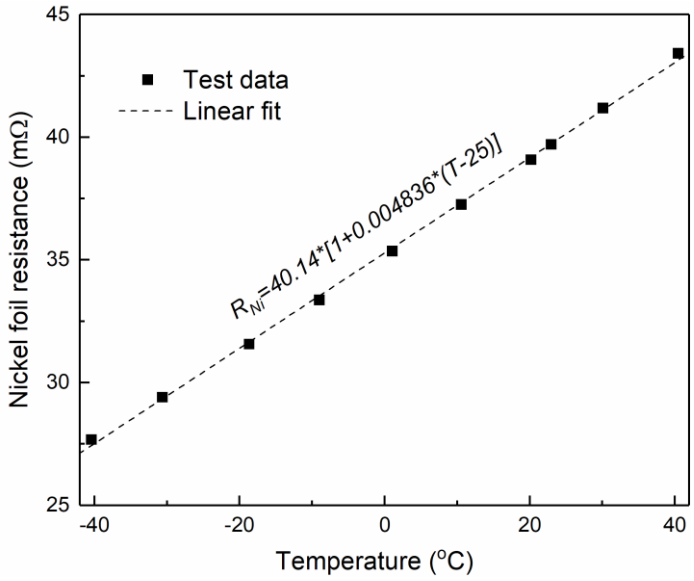

Figure S5. Linear dependence of Ni foil resistance on temperature. Calibrated overall Ni foil resistance (two foils in parallel connection) at different temperatures.

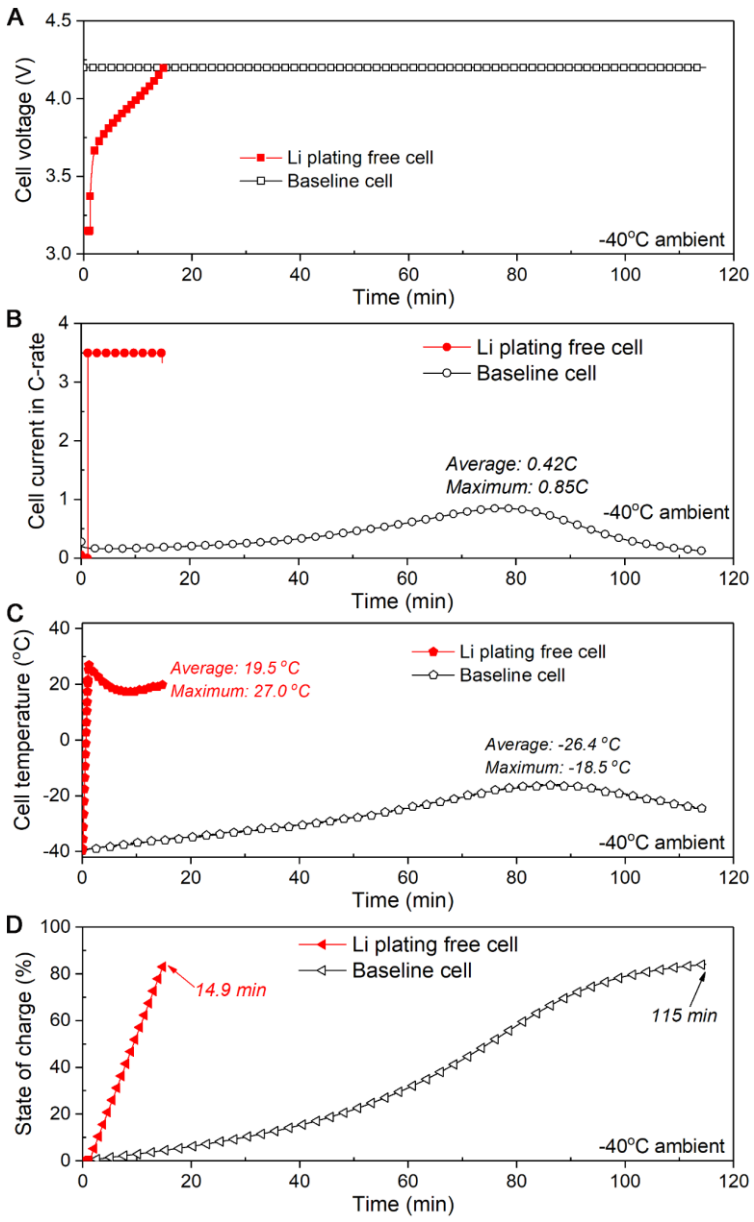

Figure S6. Lithium plating free cell vs conventional cell during charging at -40ºC. (A) voltage, **(B)** current, **(C)** surface temperature, and **(D)** state of charge for cells charging at -40ºC. The lithium plating fee cell enables 7.6x reduction of charging time compared with the baseline cell.

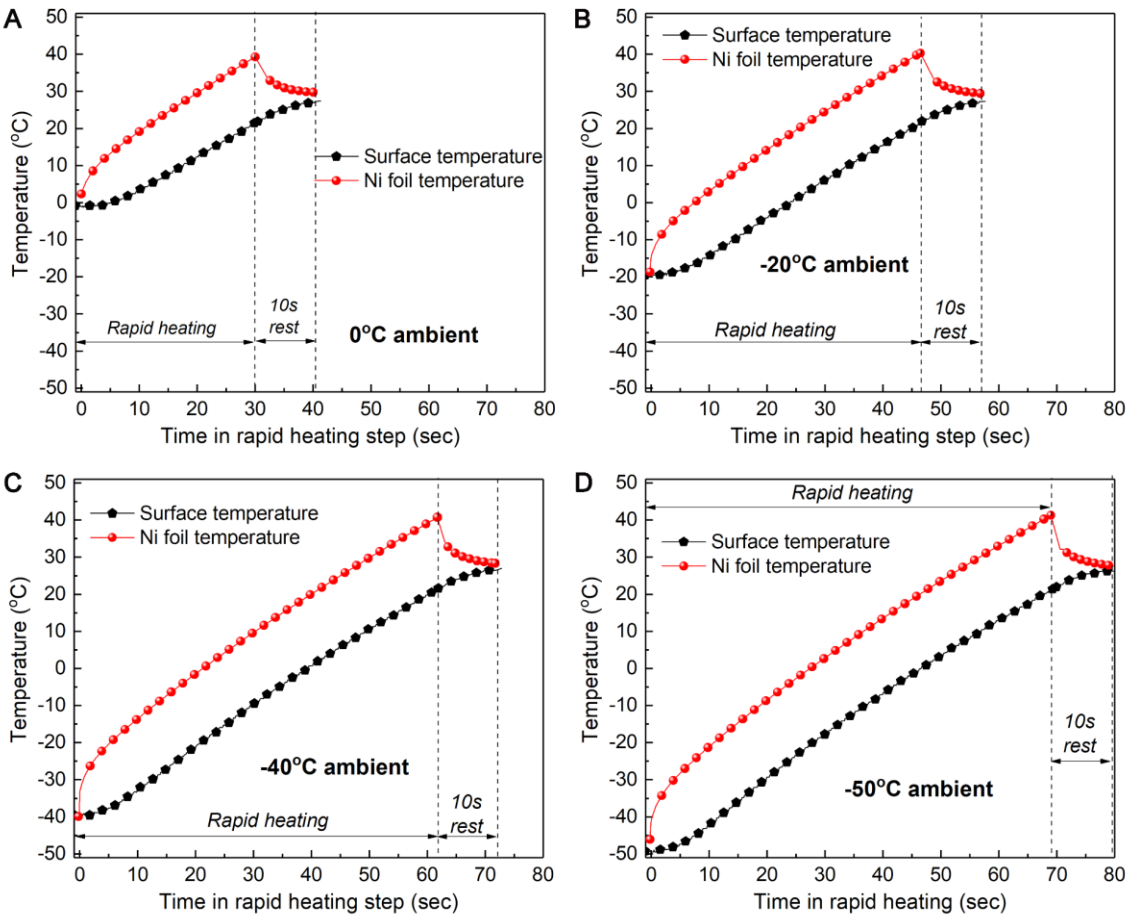

Figure S7. Evolutions of Ni foil temperature and cell surface temperature during rapid heating at different ambient temperatures. (A) 0°C; **(B)** -20°C; **(C)** -40°C and **(D)** -50°C. Ni foil temperature quickly drops in the 10-sec rest step after heating and meets with the surface temperature at ~27°C prior to charging in all four tests (i.e. similar starting charging condition at all ambient temperatures).

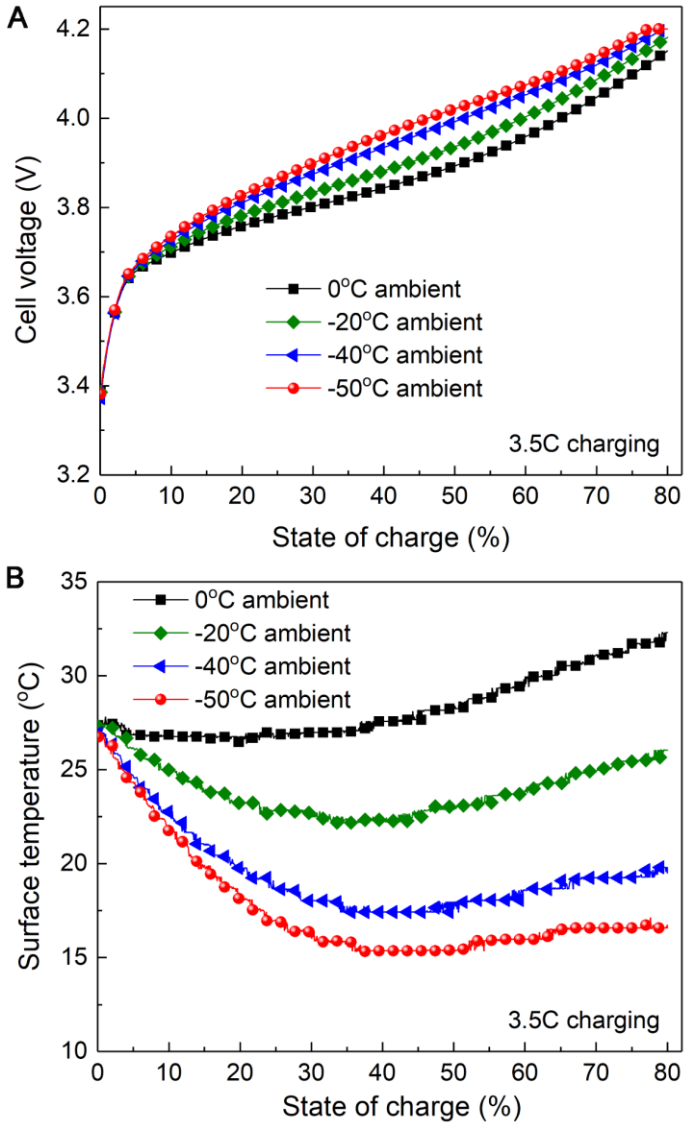

Figure S8. Unified charging voltage curve independent of ambient temperatures. Evolutions of **(A)** voltage and **(B)** surface temperature with state of charge in the 3.5C charging process after rapid heating from different ambient temperatures. The voltage curves are quite similar despite the huge difference in ambient temperature.

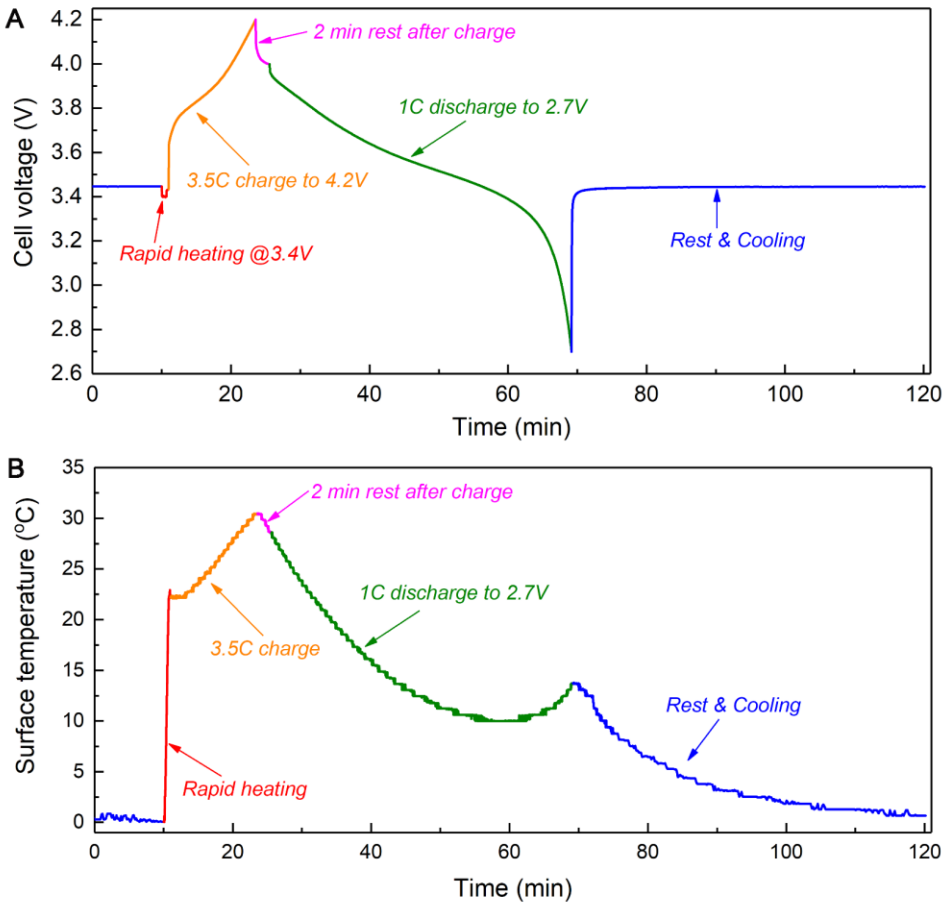

Figure S9. Protocols for 3.5C fast charging cycling test at 0°C of the lithium plating free cell. Evolution of **(A)** voltage and **(B)** surface temperature in one cycle. A rapid heating step with a constant voltage of 3.4V was applied at the beginning of each cycle, and was terminated when surface temperature reached 20°C, followed by 10-sec thermal relaxation. The cell was then charged at a constant current of 3.5C to 4.2V, followed by 2-min rest and then discharged at 1C to 2.7V, then cooled down to 0°C before performing the next cycle.

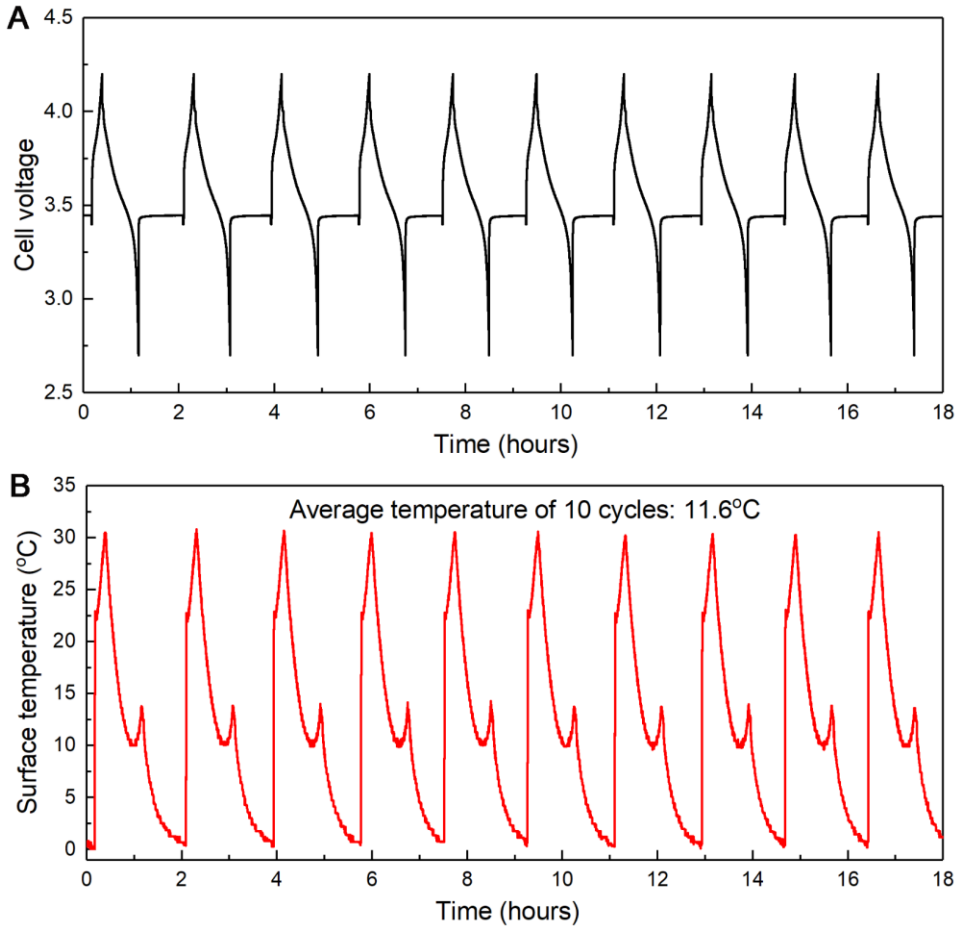

Figure S10. Voltage and temperature evolutions during 3.5C fast charging cycling of the lithium plating free cell at 0°C. Evolutions of **(A)** voltage and **(B)** surface temperature in 10 consecutive cycles.

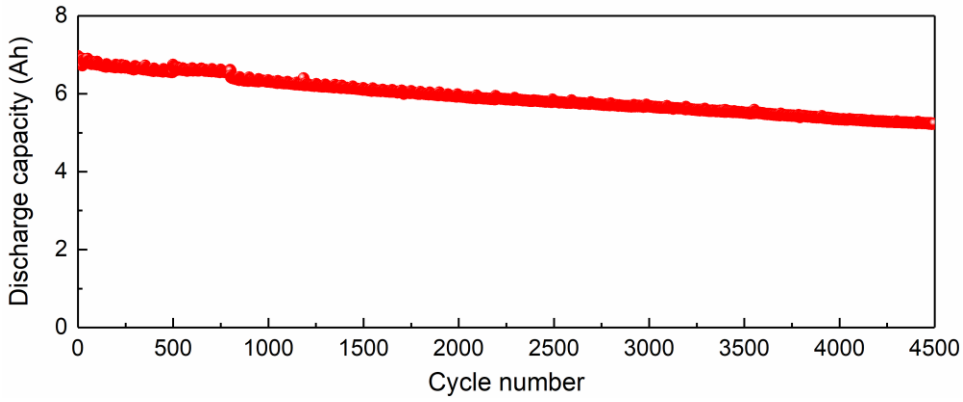

Figure S11. Discharge capacity @ 1C of each cycle during 3.5C fast charging cycling at 0°C of the lithium plating free cell.

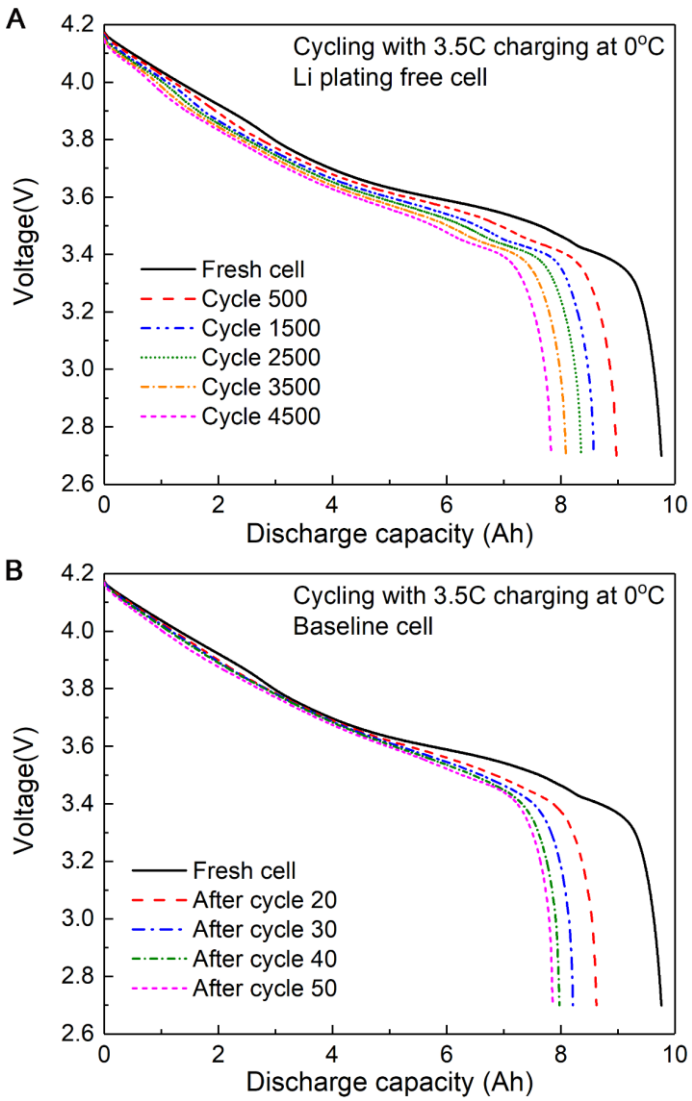

Figure S12. C/3 discharge curves of aged cells in reference performance tests (RPTs). (A) lithium plating free cell, **(B)** baseline cell. RPTs were performed by raising cell temperature to 25°C, charging at a constant current of C/3 to 4.2V followed by a constant voltage of 4.2V until current below C/20, resting for 1 hour, discharge at a constant current of C/3 to 2.7V.

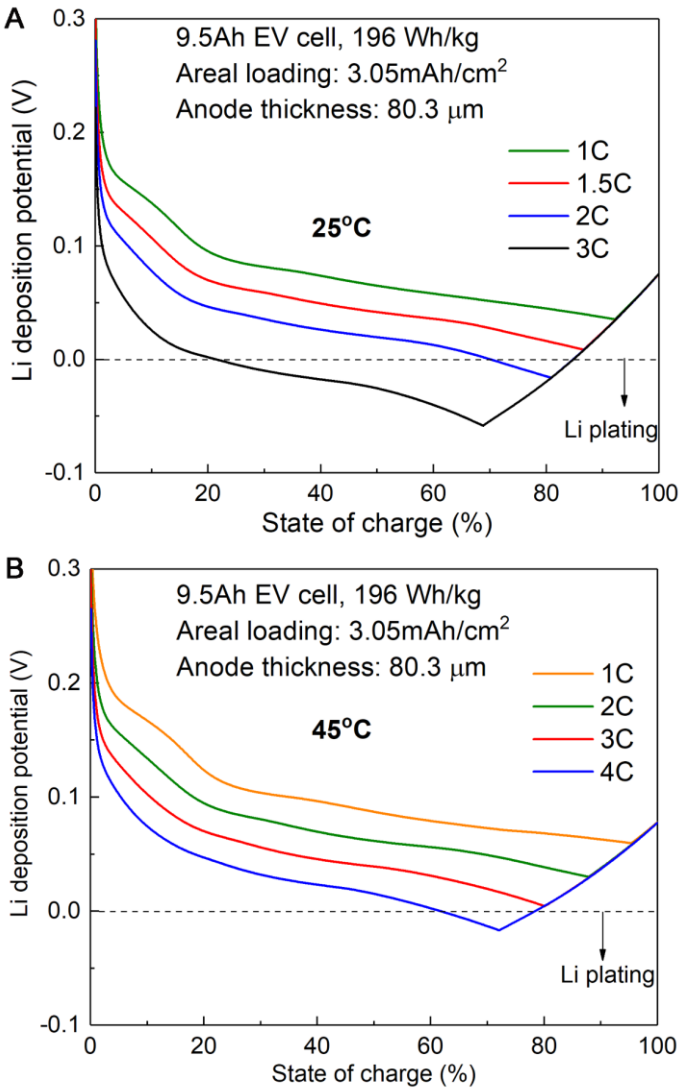

Figure S13. Maximum charge rate of high energy cells with thick electrodes. Simulation results on evolutions of Li deposition potential (LDP) during charging of a 9.5Ah high energy cell with different C-rates at **(A)** 25°C and **(B)** 45°C. This cell has 1.65 times areal loading and thickness in both anode and cathode compared with the PHEV cells in this work. All model parameters are kept the same as the calibrated PHEV cell in *SI Appendix*, Fig. S3. lithium plating is expected to occur when LDP<0V. The increase of electrode thickness leads to larger electrolyte transport resistance and thus makes the cell more prone to lithium plating.